International Journal of Rock Mechanics and Mining Sciences 117 (2019) 11–19

Contents lists available at ScienceDirect

International Journal of Rock Mechanics and Mining Sciences

journal homepage: www.elsevier.com/locate/ijrmms

Mechanical property and thermal damage factor of limestone at high temperature

Jian Yang[a,b], Li-Yun Fu[c,*], Weiqiang Zhang[d], Zhiwei Wang[b,e]

[a] State Key Laboratory of Ore Deposit Geochemistry, Institute of Geochemistry, Chinese Academy of Sciences, Guiyang, 550081, China
[b] University of Chinese Academy of Sciences, Beijing, 100049, China
[c] School of Geosciences, China University of Petroleum (East China), Qingdao, 266580, China
[d] School of Resources and Geosciences, China University of Mining and Technology, Xuzhou, 221116, China
[e] Key Laboratory of Petroleum Resource Research, Institute of Geology and Geophysics, Chinese Academy of Sciences, Beijing, 100029, China

ARTICLE INFO

Keywords:
Limestone
High temperature
Thermal damage factor: elastic modulus
Effective solid matrix

ABSTRACT

Experiments with ten groups of limestone specimens (four samples per group) under ten specific temperatures, 25 °C, 100 °C, 200 °C, 300 °C, 400 °C, 500 °C, 600 °C, 700 °C, 800 °C, and 900 °C, show that the high-temperature effect on the elastic modulus of rocks conforms to thermoelastic responses with a quadratic temperature function. The thermal damage factor can be reduced, by ignoring the effect of Poisson's ratios and densities, to simply a ratio of the *P*-wave velocities before and after high-temperature treatments. Based on the collected experimental data, we correlate the *P*-wave velocities change rate with both the peak compressive strength and effective solid matrix. It demonstrates that the high-temperature effect on the thermal damage factor can be directly expressed as the rate of change in the peak compressive strength and effective solid matrix. All these properties (thermal damage factor calculated by the *P*-wave velocity, peak compressive strength, and effective solid matrix) share a similar exponential trend with increasing temperature. The rates of change in the elastic modulus, *P*-wave velocity, peak compressive strength, and effective solid matrix also exhibit a similar powerful trend with increasing temperature. This study provides insight into the detailed characteristics of thermal damage related to the mechanical property of limestones exposed to high temperature.

1. Introduction

High-temperature rock mechanics has been widely used in engineering fields, such as coal mining,[1] geothermal reservoirs and extraction of geothermal energy,[2] building materials,[3] stability analysis of constructions exposed to fire,[4] underground coal gasification,[5] nuclear waste storage,[6] and rock drilling.[7,8] The mechanical properties of rocks change significantly at high temperature, which has been widely studied and documented. In general, wave velocities decrease as the temperature increases,[9–11] with the rate of decrease increasing with temperature.[12,13] Experiments[14] with three types of rocks (marble, limestone, and sandstone) show that the peak compressive strengths vary significantly at high temperature, with the overall trends decreasing as the temperature increases. Elastic modulus are sensitive to high temperature, generally decreasing with increasing temperature.[15–17] Controversial issue comes to the high-temperature effect on the Poisson's ratio, for example with no effect by temperature,[18,19] and increasing[20] or decreasing[21] the Poisson's ratio of granite with temperature, possibly because of differences in instruments, methods, or the diversity of samples. The porosity of rocks usually increases with temperature due to the expansion of mineral particles,[22,23] but decreases with increasing confining pressure.[24,25] It is obvious that the high-temperature effect on the mechanical property of rocks varies with different types of rocks and their diversities in physical property. At present, however, we still lack a convincing and consistent explanation for the high-temperature effect. In this study, more quantitative assessments will be conducted on the high-temperature effect by means of a thermal damage factor.

Thermal damage factor is a key index to depict the high-temperature effect on the mechanical property of rocks, and becomes a research focus recently. Thermal damage is first introduced by Dougill et al.[26] to the mechanics of rock materials. It has been widely studied in rock mechanics since then, for example, acoustic emissions and thermal cracking of granite at high temperature and pressure,[27] variations in the *P*-wave velocity of iron-bearing olivine at different temperatures under the ambient pressure,[28,29] thermal damage factors for the *P*-wave

* Corresponding author.
E-mail address: lfu@mail.iggcas.ac.cn (L.-Y. Fu).

https://doi.org/10.1016/j.ijrmms.2019.03.012
Received 13 September 2018; Received in revised form 7 January 2019; Accepted 10 March 2019

velocity and elastic modulus of limestone,[30] and uniaxial compressive strength and mechanical parameters of sandstone during and after high-temperature treatments.[31] In this study, we present a comprehensive investigation on the thermal damage factor of limestone, especially related to the peak compressive strength and effective porosity.

Limestone is one of the most common types of sedimentary rocks, distributing over a variety sources and probably differing considerably in physical microstructures and chemical compositions. Considerable progress has been made in the thermal properties of limestone attributed to previous research works, with much focusing on the heat-related physical and mechanical characteristics, for example, thermal effects on the compression strength, ultimate compression strain, and color and mass loss of four limestones extracted from the Yucatan Peninsula at heating from room temperature to 600 °C,[32] thermal effects on the pore distribution, mechanics, and acoustic emission of limestone under different temperatures heating,[33] thermal influences on the microstructure of limestone by XRD, SEM and TG-DSC experiments exposed to 800 °C,[34] thermal damages with various physical and mechanical properties of limestone at elevated temperatures including microstructure, bulk density, effective porosity, *P*-wave velocity, uniaxial compressive strength, Brazilian tensile strength, modulus of elasticity, and Shore hardness.[35–37] Most of the above studies on limestone contribute to thermal effects on the physical and mechanical properties, but with few investigating the thermal damage factor of limestone at high temperature.

In this article, we calculate thermal damage factors by correlating the *P*-wave velocities with changes in the peak compressive strength and effective solid matrix based on the collected experimental data. The detailed characteristics of thermal-damage effects is presented with a discussion on the thermal damage mechanism according to observed variations in the mechanical properties of limestone, including elastic modulus, *P*-wave velocity, peak compressive strength, and effective solid matrix. In conclusion, the thermal damage factor can be expressed in terms of the peak compressive strength and the rate of change in the effective solid matrix, much better than the rate of change in the *P*-wave velocity. The high-temperature effect on the elastic modulus follows quadratic thermoelastic prediction, possibly providing a theoretical basis for high-temperature rock mechanics with respect to the mechanical properties of limestone.

2. Theoretical background

2.1. Thermoelasticity equations

Based on the Clausius inequality, the stress tensor σ_{ij} is expressed as

$$\sigma_{ij} = \frac{\partial \Psi}{\partial \gamma_{ij}}, \tag{1}$$

where γ_{ij} is the strain tensor. $\Psi = \Psi(\gamma_{ij}, \theta^*)$ is the Helmholtz free energy per unit volume, where the dimensionless temperature increment θ^* is defined as $\theta^* = \theta/T_0$ with the temperature increment $\theta = T - T_0$ (T and T_0 are the absolute and reference temperatures, respectively). To obtain the constitutive thermoelasticity equations for an isotropic material, the Helmholtz free energy density is expanded in a power series with respect to γ_{ij} and θ^*, as the following form[38,39]

$$\begin{aligned}\Psi(\gamma_{ij}, \theta^*) = {} & a_0 + a_1 I_1 + a_2 I_2 + a_3 I_3 + a_4 \theta^* + a_5 I_1^2 \\ & + a_6 \theta^{*2} + a_7 I_1 \theta^* + a_8 I_1^3 + a_9 I_1 I_2 + \cdots,\end{aligned} \tag{2}$$

where $a_0, a_1, \cdots a_9$ are material constants, and I_1, I_2, I_3 are invariants of strain tensors, which are expressed as

$$\begin{cases} I_1 = \gamma_{ij} \\ I_2 = \frac{1}{2}(\gamma_{ii}\gamma_{jj} - \gamma_{ij}\gamma_{ji}) \\ I_3 = det\gamma_{ij}\,. \end{cases} \tag{3}$$

By ignoring terms higher than the third order of θ^* and taking the second order of γ_{ij} for Eq. (2), $\Psi(\gamma_{ij}, \theta^*)$ is expressed in the following forms:

$$\begin{aligned}\Psi(\gamma_{ij}, \theta^*) = {} & a_0 + a_1 I_1 + a_2 I_2 + a_4 \theta^* + a_5 I_1^2 + a_6 \theta^{*2} \\ & + a_7 I_1 \theta^* + a_{10} I_1 \theta^{*2} + a_{11} I_2 \theta^* + a_{12} \theta^{*3} + a_{13} I_1^2 \theta^*\end{aligned} \tag{4}$$

The elastic stress component is given by the following relation[40,41]

$$\sigma_{ij} = \frac{\partial \Psi}{\partial \gamma_{ij}} = \frac{\partial \Psi}{\partial I_1}\frac{\partial I_1}{\partial \gamma_{ij}} + \frac{\partial \Psi}{\partial I_2}\frac{\partial I_2}{\partial \gamma_{ij}} + \frac{\partial \Psi}{\partial I_3}\frac{\partial I_3}{\partial \gamma_{ij}}\,. \tag{5}$$

Substituting Eq. (4) into (5), we have

$$\begin{aligned}\sigma_{ij} = {} & a_1 \delta_{ij} + [(a_2 + 2a_5) + (a_{11} + 2a_{13})\theta^*]\gamma_{kk}\delta_{ij} \\ & - (a_2 + a_{11}\theta^*)\gamma_{ij} + (a_7 + a_{10})\theta^*\delta_{ij}\,,\end{aligned} \tag{6}$$

where δ_{ij} is the Kronecker delta, and a_1 is zero in the natural state and is regarded as the initial normal stress.[42]

By introducing the Lame's constants μ, λ and thermoelastic coupling coefficient β, the temperature-dependent constitutive equation is written as

$$\sigma_{ij} = (\lambda_1 \theta^* + \lambda_0)\gamma_{kk}\delta_{ij} + 2(\mu_1 \theta^* + \mu_0)\gamma_{ij} - (\beta_1 \theta^* + \beta_0)\theta\delta_{ij}\,, \tag{7}$$

where $\beta_0 = -\frac{a_7}{T_0}$ $\lambda_0 = a_2 + 2a_5$, and $\mu_0 = -\frac{a_2}{2}$ are their initial values at the reference temperature T_0, and the same forms of the material constants $\beta_1 = -\frac{a_{10}}{T_0}$, $\lambda_1 = 2a_{13} + a_{11}$, and $\mu_1 = -\frac{a_{11}}{2}$ are considered as the influencing factors of temperature deviation.

The general formula of Eq. (7) as the temperature-dependent constitutive equation can be rewritten in a concise form:

$$\sigma_{ij} = \lambda(\theta)\gamma_{kk}\delta_{ij} + 2\mu(\theta)\gamma_{ij} - \beta(\theta)\theta\delta_{ij}\,, \tag{8}$$

where the temperature-dependent material constants can be expressed as

$$\begin{cases} \lambda(\theta) = \lambda_1\theta^* + \lambda_0 = \lambda \\ \mu(\theta) = \mu_1\theta^* + \mu_0 = \mu \\ \beta(\theta) = \beta_1\theta^* + \beta_0 = \beta\,. \end{cases} \tag{9}$$

For simplicity, Wang[43] introduces the following form:

$$\begin{cases} \eta_v = \frac{\lambda_1 + \mu_1}{\lambda_0 + \mu_0} \\ \xi_v = \frac{-\lambda_1\left(\mu_0/\lambda_0\right) + \mu_1}{\lambda_0 + \mu_0}\,. \end{cases} \tag{10}$$

And the power series expansion with respect to η_v and ξ_v by

$$\upsilon = \frac{1}{2}\frac{\lambda_0}{\lambda_0 + \mu_0}(1 - \xi_v\theta^* + \xi_v\eta_v\theta^* - \xi_v{\eta_v}^2\theta^{*3} + \cdots)\,. \tag{11}$$

By taking the two preceding items in Eq. (11), the elastic modulus can be expressed in a quadratic temperature function as

$$E = E_2\theta^{*2} + E_1\theta^* + E_0\,, \tag{12}$$

where the material constants E_2, E_1, E_0 are written as

$$\begin{cases} E_2 = 2\mu_1\nu_1 \\ E_1 = 2(\mu_1 + \mu_1\nu_0 + \mu_0\nu_1) \\ E_0 = 2(\mu_0 + \mu_0\nu_0)\,. \end{cases} \tag{13}$$

2.2. Thermal damage factor

Zhao et al.[44] defined the thermal damage factor of rocks by an elastic strain method. For completely elastic materials, the relationship between the strain ε_0 and the stress σ can be simply expressed as

$$\sigma = E_0\varepsilon_0\,, \tag{14}$$

where E_0 is the elastic modulus.

When rock materials are damaged, the strain-stress relationship is

destroyed, leading to an updated version of Eq. (14) as

$$\sigma = E_0(1 - F)\varepsilon_1 , \tag{15}$$

where F is defined as the thermal damage factor. $E_T = E_0(1 - F)$ is the new elastic modulus of materials damaged by temperature treatment. Therefore, the thermal damage factor F is obtained as follows:

$$\mathrm{F}(T) = 1 - \frac{E_T}{E_0} \tag{16}$$

According to the elastic coefficients defined previously, E can be expressed as

$$E = \frac{\rho V_p^2(1 + \nu)(1 - 2\upsilon)}{1 - \upsilon} , \tag{17}$$

where V_p is the P-wave velocity, υ and is the Poisson's ratio, and ρ is the density.

Substituting Eq. (16) into (17), we have

$$\mathrm{F}(T) = 1 - \left(\frac{V_T}{V_0}\right)^2 \frac{\rho_T(1 + \nu_T)(1 - 2\nu_T)(1 - \nu_0)}{\rho_0(1 - \nu_T)(1 + \nu_0)(1 - 2\nu_0)} , \tag{18}$$

where the subscript T denotes the damaged rock at the heating temperature, and the subscript 0 corresponds to the undamaged rock at the room temperature.

By ignoring the terms ρ and ν, Eq. (18) is further reduced to

$$\mathrm{F}(T) = 1 - \left(\frac{V_T}{V_0}\right)^2 \tag{19}$$

We see that the thermal damage factor can be approximately calculated by the rate of wave velocities before and after high-temperature treatments. Two hypotheses are adopted for simplification of the thermal damage factor: samples undamaged at the room temperature and experienced same thermal elastic damage by 25°–900 °C.[30]

3. Experimental materials and methods

The samples of grey red limestone, used in the reviewed experiment, are collected from Linyi City, Shandong Province, eastern China, with some oolitic veins observed on the surface of these samples. Test specimens with an average bulk density of 2.710 g/cm3 at room temperature are normatively cut into Φ50 × 100 mm cylinders with a uniform texture. The limestone specimens consist mainly of calcite and dolomite, as determined by X-ray diffraction.[17]

Technical parameters of experimental instruments are given in Table 1. The entire experimental techniques, as described in Zhang et al.,[17,30,45] include the coupling measurements for P-wave velocities by using Vaseline as coupling material; elastic modulus by uniaxial compressive test inside the linear deformation stage of a stress-strain curve, and Poisson's ratio as an absolute value of the ratio of transverse to that longitudinal strains.

According to the experimental procedures as described in Zhang et al.,[17,30,45] all initial properties of samples are measured to establish a comparison basis for thermal treatments. Ten groups of limestone samples (four samples per group) are then heated to ten temperatures: 25 °C, 100 °C, 200 °C, 300 °C, 400 °C, 500 °C, 600 °C, 700 °C, 800 °C, and 900 °C, followed by the measurement of physical and mechanical properties. The thermal treatment consists of three stages: sample heating to the target temperature at a low heating rate of 5 °C/min, temperature maintaining for 2 h to ensure full uniform heating, and sample cooling to room temperature at a rate below 5 °C/min to prevent thermal shock during heating and cooling. All the physical and mechanical parameters are measured again after cooling, followed by scanning electron microscopy and mercury injection tests.

4. Results and discussion

Experimental data of limestone show significant changes in the physical and mechanical properties before and after thermal treatments, especially for the P-wave velocity, peak compressive strength, elastic modulus, porosity, and Poisson's ratio. A comprehensive analysis for the detailed characteristics are presented as follows.

4.1. Elastic modulus

As shown in Fig. 1 for the experimental data of elastic modulus with temperature, we see that the elastic modulus reaches its maximum of 73.14 GPa at room temperature and decreases significantly from 100 °C to 200 °C, followed by a relatively slow reduction from 200 °C to 600 °C, even more slowly at temperatures after 600 °C. This implies that the emerging and rapid expansion of microcracks, because of internal thermal stress appearing at higher temperature, significantly reduce the elastic modulus to some degree. That is, high temperature can damage rocks. The thermal-induced variations in elastic modulus can be empirically fitted by a quadratic temperature function as follows,

$$E = 77.716 - 0.172T + 9.541{*}10^{-5}T^2 . \tag{20}$$

The correlation coefficient of the fitting up to 0.986, indicating that the elastic modulus could be represented by a quadratic thermo-elasticity equation, like Eq. (12).

We use the change rate K_e to characterize the thermal-induced variations in elastic modulus, which is calculated by the ratio of elastic modulus before and after thermal treatments as follows,

$$K_e = \frac{E_0 - E_T}{E_0} , \tag{21}$$

where the subscript T denotes the elastic modulus after heating at a high temperature, and the subscript 0 corresponds to the initial elastic modulus.

Fig. 2 shows the change rate of elastic modulus with temperature, which can be well fitted by the following empirical curve with the correlation coefficient up to 0.961,

Table 1
Experimental instruments and main technical parameters.

Properties	Test instruments	Technical parameters
P-wave velocities	RS-ST01C integration digital acoustic detector	Two transducers: transmitter and receiver
Porosity	AutoPore IV 9510 automatic mercury injection apparatus	Working pressure: 0.0–400.0 MPa Pore size range: 0.003–250 μm
Peak compressive strength, elastic modulus, and Poisson's ratio	WES-D1000 electro-hydraulic servo universal testing machine	Uniaxial compressive test with a loading rate of 500 N/S
Microstructure	FEI QuantaTM 250 scanning electron microscope	Resolution less than 3.5 nm Accelerating voltage: 0.2 kV–30 kV
Heat treatment	CTM300A high-temperature furnace	Temperature range: 1000 °C Precision: 5 °C Resolution: 1 °C Heating rate: 5 °C/min

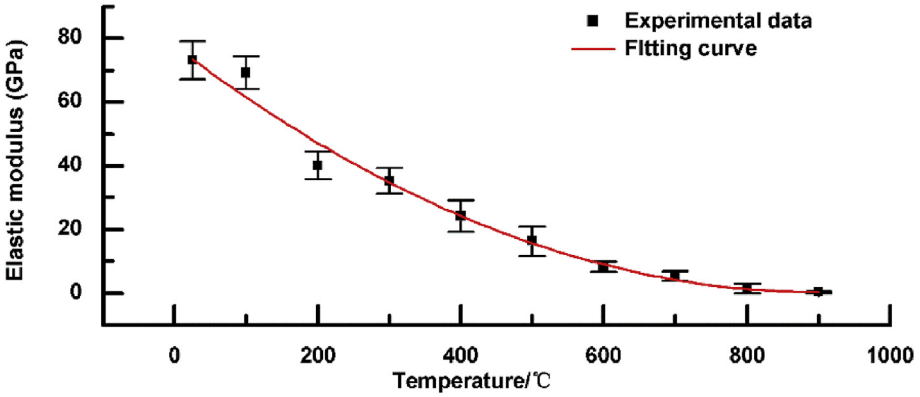

Fig. 1. Variations in the elastic modulus of limestone with temperature.

$$K_e = -0.391 + 0.900T^{0.408}. \quad (22)$$

We see that the evolution of the change rate K_e with temperature, because of the same thermal damage mechanism as shown in Fig. 1, can be divided into three stages: relatively smooth change with less thermal effect at approximately linear elastic deformation stage from 25 °C to 100 °C, drastic increasing by heating temperatures from 100 °C to 200 °C, and turning to slow increasing from 200 °C to 900 °C.

4.2. P-wave velocity change rate and thermal damage factor

Wave propagation in rocks is mainly affected by mineral composition, microstructure, cementation degree, stress, and temperature. The *P*-wave velocity limestone is measured before and after heating with attempt to identify the thermal-induced velocity variations.

Likewise, we define the following change rate K_p, the ratio of wave velocities before and after thermal treatments, to describe the thermal-induced variations in the *P*-wave velocity,

$$K_p = \frac{V_0 - V_T}{V_0}, \quad (23)$$

where the subscript definition is similar to that in Eq. (21).

Fig. 3 shows the change rate of *P*-wave velocity with temperature, which can be well fitted by the following empirical curve, similar a powerful trend with temperature, with the correlation coefficient up to 0.910,

$$K_p = -0.134 + 0.003T^{0.834}. \quad (24)$$

As shown in Fig. 3, we see that the evolution of the change rate K_p with temperature can be divided into three stages: firstly, from 25 °C to 200 °C, the change rate K_p is relatively constant. In this stage, heating rock particles expand the rock, potentially create new pores[46]; however, the lengths, numbers, and areas of initial pores decrease because of thermal stress caused by rock expansion, which can also alter the pore volume. Therefore, the change rate K_p remains relatively smooth change. Secondly, from 200 °C to 700 °C, the change rate K_p increases sharply from 0.116 to 0.651, which influenced by intricate factors. Heating treatments induce clay mineral decomposition and constitution, and crystal water evaporation. Also, the degree of cementation decreases when links among particles break and new cracks are generated around the particles,[47] because the particles have insufficient room for expansion. The looser particle arrangement and increasing pores can prevent *P*-wave propagation in specimens. Besides, the different minerals constituting the heterogeneous body have different expansion coefficients at the same temperature, producing thermal stress due to their uncoordinated deformation. The elastic properties of rocks are significantly affected by the initial pores and microcracks influenced by thermal stress. Thus, initial pores changed and rock microcracks are caused by thermal stress, which significantly affects the porosity of rocks to influence the *P*-wave velocity. Therefore, the change rate K_p drastically increases in this field. Thirdly, from 700 °C to 900 °C, the change rate K_p generally increases and remains steady from 0.651 to 0.746. Within this stage, constitution water evaporation is not the primary cause, whereas thermal stress significantly affects the rocks and internal cracks gradually accumulate. Firstly, thermal decomposition begins, e.g., calcite begins to decompose, transforming to *CaO* and portlandite above 700 °C, with its overall structure collapsing through cracking at 900 °C. Secondly, above 700 °C, microcracks that begin to appear at grain to grain contacts are attributed to the thermal expansion of the crystals, resulting in macrofractures that increase the pore size; larger cracks simultaneously form when microcracks penetrate mineral particles (calcite, dolomite, etc.) and break them down into smaller particles, leaving from macrofractures, which can cause structural collapse of minerals.[23,48] Therefore, the change rate K_p changes into slow increasing within this temperature range.

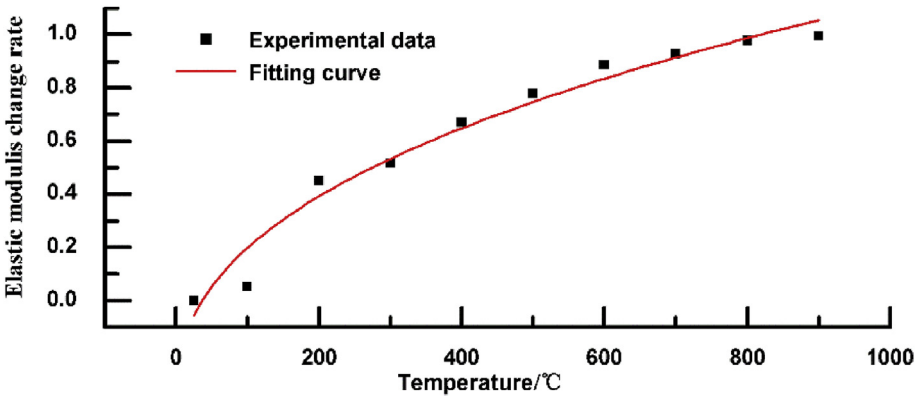

Fig. 2. Change rate of elastic modulus with temperature.

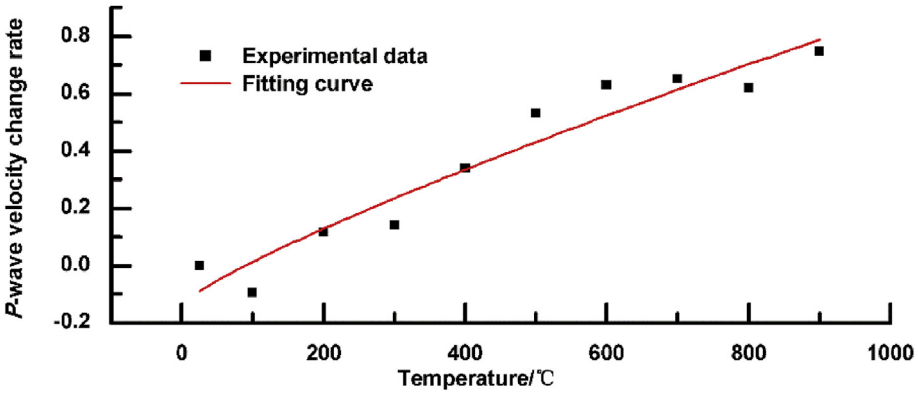

Fig. 3. Change rate of compression wave velocity with temperature.

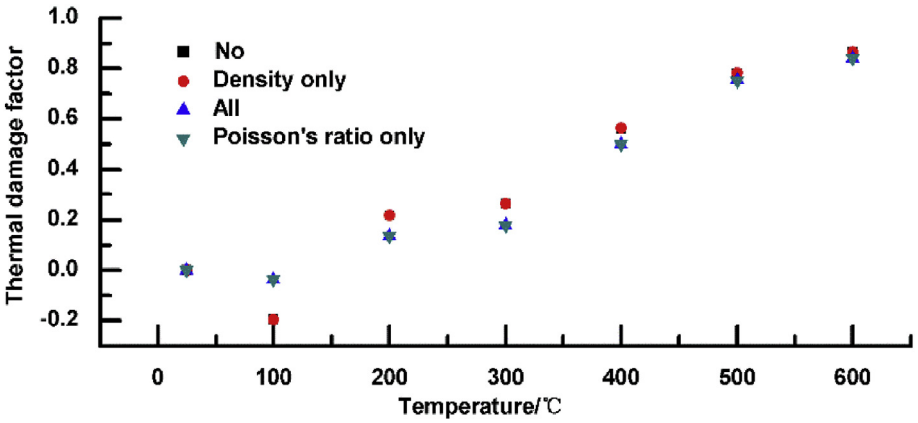

Fig. 4. Thermal damage factor calculated by equation (18) with temperature.

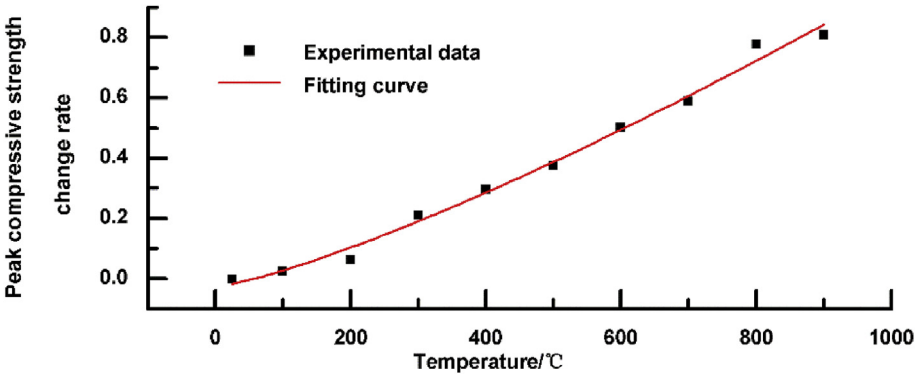

Fig. 5. Change rate of peak compressive strength with temperature.

Based on experimental results about the effect of Poisson's ratio and density on the thermal damage factors at different temperatures, as shown in Fig. 4, we see the remarkable agreement for all the points except for that at 100 °C. This can be explained by gradual evaporation due to heating of free water into steam that probably reserves in the closed pores; the absence or presence of free water could significantly influence Poisson's ratio. In addition, we see a little change in density, with its change rate merely 0.012 at 600 °C, and even 0.129 at 900 °C.[45] Therefore, the thermal damage factor can be calculated using Eq. (18), with the effect of Poisson's ratio and density ignored.

4.3. Peak compressive strength change rate and thermal damage factor

The uniaxial peak compressive strength is the peak stress that rock samples can endure from a single direction, which is one of the most significant parameters reflecting the basic mechanical properties of rocks. Such factors, for example, the peak compressive strength dependence increasing with increasing strain-rate, either linear relation or exponential trend,[49–51] decreasing with increasing temperature[52] and with increasing slenderness of the specimen,[53,54] can significant influence the peak stress. In addition, the peak compressive strength with confining pressure, which can be expressed by $^{C}/_{C_0}$ with $^{P}/_{C_0}$, where C is the peak compressive strength under confining pressure P, C_0 is the compressive strength peak at atmospheric pressure with shear strength and confining pressure negatively correlated.[55,56]

Similarly, we use the following change rate K_{peak}, the ratio of peak compressive strength before and after thermal treatments, to describe the thermal-induced variations in the peak compressive strength,

$$K_{peak} = \frac{P_0 - P_T}{P_0}, \tag{25}$$

where the subscript definition is also similar to that in Eq. (21).

Fig. 5 shows the change rate of peak compressive strength with temperature, which can be well fitted by the following empirical curve, similar a powerful trend with temperature, with the correlation coefficient up to 0.988,

$$K_{peak} = -0.027 + 1.607*10^{-4}T^{1.263}. \quad (26)$$

We see that the evolution of the change rate K_{peak} with temperature, as shown in Fig. 5, can be divided into three stages: firstly, from 25 °C to 200 °C, the change rate K_{peak} remains relatively smooth change. Within this temperature range, the outside and inside of limestone are heated unevenly, and a small number of microdefects are induced by gradually increasing temperature; in addition, $Ca(HCO_3)_2$ in the rock decomposes to CaO, CO_2, and H_2O at about 200 °C, which can change the pore volume. Considering the above-mentioned factors, the change rate K_{peak} remains almost constant. Secondly, from 200 °C to 700 °C, the change rate K_{peak} increases acutely from 0.211 to 0.588 with heating temperatures. Within this range, the change rate K_{peak} is mainly affected by the following factors. The rock expansion behavior significantly affects the properties of rocks, even when their thermal expansion is relatively small. Also, thermal stress can extend existing cracks, causing irreversible structural damage, which can decrease the peak compressive strength. Small new microcracks may emerge with the thermal stress below the ultimate compressive strength, resulting in minimal change in the peak compressive strength. Thirdly, from 700 °C to 900 °C, the change rate K_{peak} is generally huge and increases to 0.809 from 0.588. In this range, the peak compressive strength is primarily affected by thermal stress, rather than constitution water evaporation. Above 700 °C, thermal stress may significantly increase, and new microcracks and microcrack extensions may appear when the thermal stress surpasses the ultimate compressive strength or shear strength. Therefore, this leads to an obvious decrease in peak compressive strength with microstructural changes.

Fig. 6 shows the relationship between change rate of *P*-wave velocity and peak compressive strength, which can be well fitted by the following empirical curve,a powerful trend, with the correlation coefficient up to 0.897,

$$K_p = -0.339 + 1.167K_{peak}^{0.400}. \quad (27)$$

The thermal damage factors calculated by the change rate K_{peak} are shown in Fig. 7, which can be well fitted by the following empirical curve, an exponential trend with temperature, with the correlation coefficient up to 0.917,

$$F_{peak} = 1.271 - 1.497exp\left(-\frac{T}{551.950}\right). \quad (28)$$

We see that the evolution of the change rate F_{peak} with temperature, because of the same thermal damage mechanism as shown in Fig. 5, can be divided into three stages: relatively smooth change with less thermal effect from 25 °C to 200 °C, drastic increasing caused by the loss of crystal and structural water, decomposition, and thermal stress with heating temperatures from 200 °C to 700 °C, and turning to slow increasing mainly influenced by thermal stress from 700 °C to 900 °C.

4.4. Effective solid matrix change rate and thermal damage factor

The total porosity consists of isolated porosity and connected porosity (the connected porosity includes dead-end porosity and transport porosity),[57] the effective porosity is generally defined for solute transport as that portion of the soil or rock through which chemicals move, or that portion of the media that contributes to flow.[58,59] That is, the effective porosity not includes isolated porosity and dead-end porosity. The porosity tested by automatic mercury injection apparatus obtains the effective porosity. In order to conveniently study the property of porosity heated to high temperature, we introduce the concept of effective solid matrix, which pluses the value of the effective porosity makes one.

Also, we define the following change rate K_s, the ratio of effective solid matrix before and after thermal treatments, to describe the thermal-induced variations in the effective solid matrix,

$$K_s = \frac{S_0 - S_T}{S_0}, \quad (29)$$

where the subscript definition is also similar to that in Eq. (21).

Fig. 8 shows the change rate effective solid matrix with temperature, which can be well fitted by the following empirical curve, similar a powerful trend with temperature, with the correlation coefficient up to 0.968,

$$K_s = -5.426*10^{-4} + 8.908 * 10^{-9}T^{2.264}. \quad (30)$$

We see that the evolution of the change rate K_s with temperature, as shown in Fig. 8, can also be divided into three stages: firstly, from 25 °C to 200 °C, the change rate remains K_s relatively constant with some fluctuation. Within this range, rocks expand as their particles are heated, which may create new pores[32]; also, the free water gradually forms steam and may escape from the open pores, and gas may be released from isolated pores after heating, potentially increasing the pore volume. Besides, bound water can only escape if the temperature is above 100 °C, and weakly bound water can completely escape at about 150 °C. Considering the above factors, the pore volume may increase or decrease, causing the change rate K_s to remain relatively smooth change with temperature. Secondly, from 200 °C to 700 °C, the change rate K_s increases drastically from 0.00572% to 2.275%. This stage can be divided into two parts as well: from 200 °C to 500 °C and from 500 °C to 700 °C. From 200 °C to 500 °C, the change rate K_s slowly increases with temperature, because of strongly bound water completely escaping

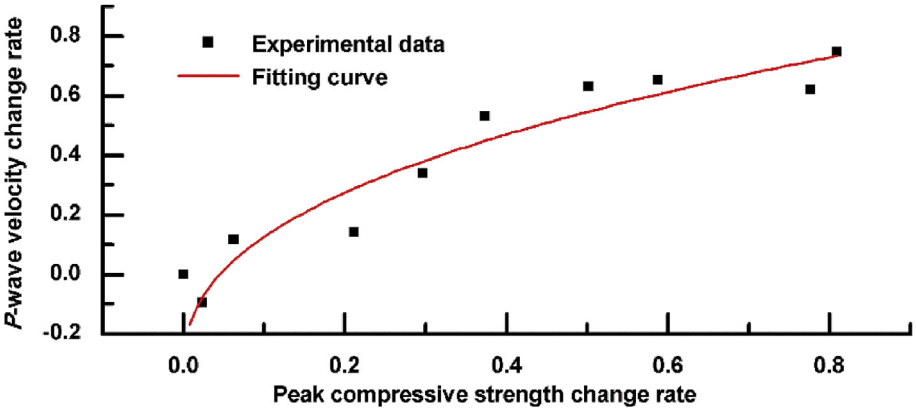

Fig. 6. Change rate of *P*-wave velocity with peak compressive strength.

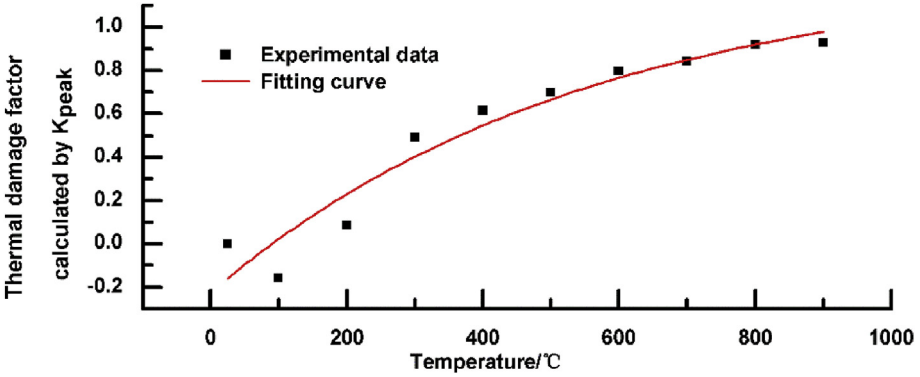

Fig. 7. Thermal damage factor calculated by the change rate of peak compressive strength with temperature.

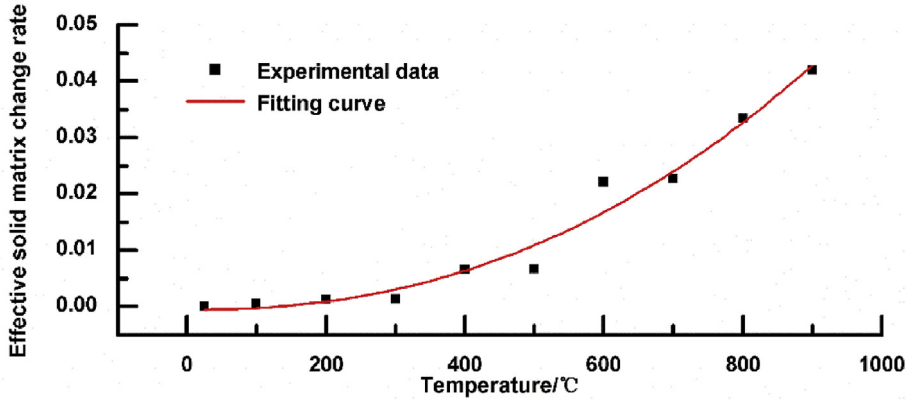

Fig. 8. Change rate of effective solid matrix with temperature.

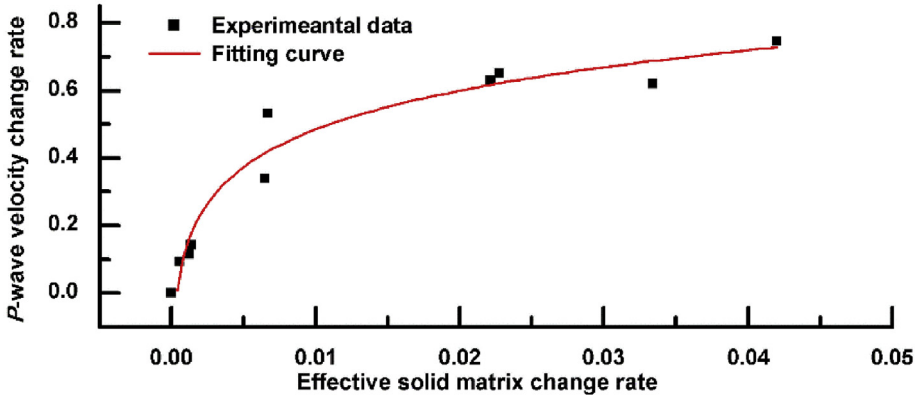

Fig. 9. Change rate of *P*-wave velocity with effective solid matrix.

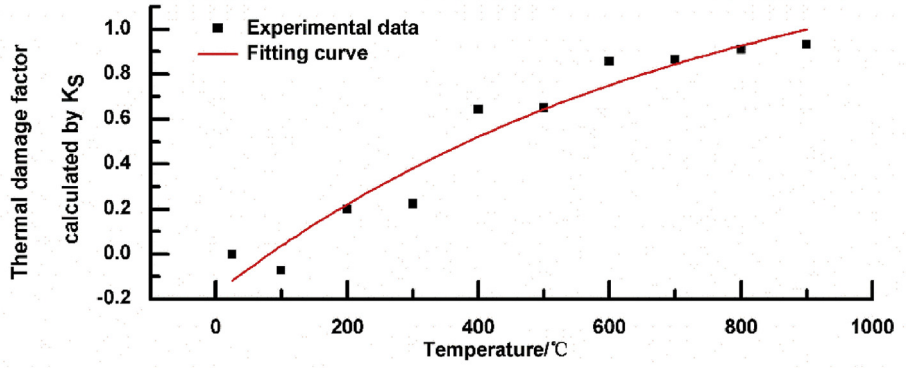

Fig. 10. Thermal damage factor calculated by the change rate of effective solid matrix with temperature.

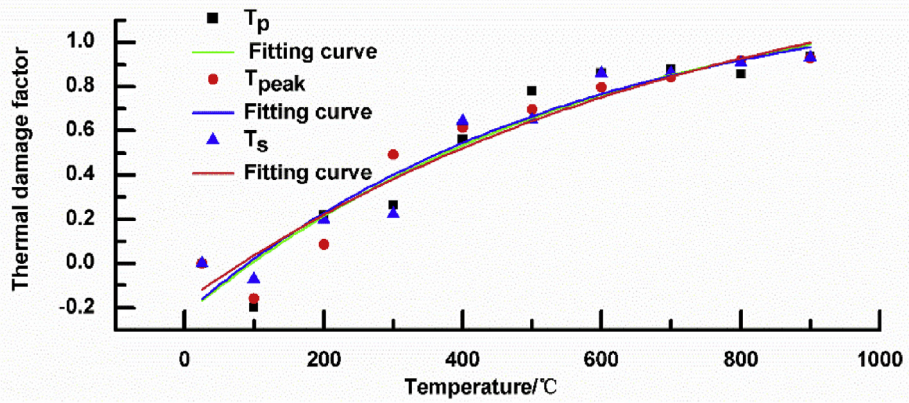

Fig. 11. Thermal deformation factor calculated by the change rate of *P*-wave velocity, peak compressive strength, and effective solid matrix with temperature.

at approximately 200 °C–300 °C while crystal water escaping below 400 °C. That is, thermal stress appears but remains small. From 500 °C to 700 °C, the change rate K_s sharply increases with temperature from 500 °C to 600 °C, which can be attributed to increasing thermal stress. However, the change rate K_s remains constant with increasing temperature from 600 °C to 700 °C, which can be explained by volume reduction caused by $MgCO_3$ decomposition at about 600 °C.[60,61] Thirdly, from 700 °C to 900 °C, the change rate K_s generally drastically increases with temperature and reaches 4.200% from 2.275%. Within this range, the thermal stress increases with porosity, which can be explained by increasing pores due to thermal $CaCO_3$ decomposition in the limestone at 700 °C.[61] Scanning electron microscopy indicates that the integrity of the mineral crystals was destroyed when the temperature reached 600 °C, which increased porosity as cracks developed and larger holes appeared.[45] In conclusion, internal moisture continuously escapes from the samples and thermal stress appears as the temperature increases, increasing microcracks, changing the internal rock composition, including $MgCO_3$ decomposition into MgO and CO_2 at about 600 °C, the calcite ($CaCO_3$) starting to decompose into CaO and CO_2 at 700 °C and completely decomposition at 870 °C, the dolomite ($CaMg[CO_3]_2$) decomposition into MgO, CO_2, and $CaCO_3$ at about 750 °C,[62] and increasing its internal porosity.

Fig. 9 shows the relationship between change rate of *P*-wave velocity and effective solid matrix, which can be well fitted by the following empirical curve, similar a powerful trend, with the correlation coefficient up to 0.942,

$$K_p = -120.818 + 122.133K_s^{0.00149}. \quad (31)$$

The thermal damage factors calculated by the change rate F_s are shown in Fig. 10, which can be well fitted by the following empirical curve, a similar exponential trend with temperature, with the correlation coefficient up to 0.924,

$$F_s = 1.492 - 1.655exp\left(-\frac{T}{740.758}\right). \quad (32)$$

We see that the evolution of the change rate F_s with temperature, because of the same thermal damage mechanism as shown in Fig. 8, can also be divided into three stages: relatively constant with some fluctuation from 25 °C to 200 °C, sharply increasing caused by thermal stress appearing and increasing, and volume reduction affected by $MgCO_3$ decomposition at about 600 °C from 200 °C to 700 °C, changing into slow increasing attributed to increasing pores caused by slight $CaCO_3$ decomposition in the limestone at 700 °C, bulk decomposition occurring at 870 °C, and simultaneous formation of MgO, CO_2, and $CaCO_3$ accompanied dolomite decomposition at about 750 °C from 700 °C to 900 °C.[61,62]

We see that the thermal damage factor calculated by the change rate of *P*-wave velocity, peak compressive strength, and effective solid matrix with temperature, as shown in Fig. 11, exhibit similar exponential trends with temperature, suggesting that the change rate of peak compressive strength and effective solid matrix can effectively express the thermal damage factor, and the correlation fitting coefficients of the curves are 0.899, 0.917, and 0.924, respectively. That is, the thermal damage factor expressed by the change rate of peak compressive strength and effective solid matrix is much better than by the change rate of *P*-wave velocity. In addition, the relationships between the peak compressive strength, effective solid matrix, and thermal damage factor can be considered as empirical formulas, which are useful for future relevant research on thermal damage of limestone exposed higher temperature.

5. Conclusion

The high-temperature effect on the elastic modulus of limestone follows quadratic thermoelastic prediction, with the fitting correlation coefficient to experimental data up to 0.98.

The change rate of elastic modulus, *P*-wave velocity, peak compressive strength, and effective solid matrix share similar exponential trends with temperature, with their fitting correlation coefficients up to 0.961, 0.910, 0.988, and 0.968, respectively.

Based on the crossplot of *P*-wave velocities with peak compressive strengths/effective solid matrices at different temperature, the thermal damage factor can be expressed by the change rate of peak compressive strength and effective solid matrix, much better than the change rate of *P*-wave velocity.

High temperature significantly influences the mechanical properties of limestone and causes rock damaging, accumulating the thermal damage factor gradually with increasing temperature.

Acknowledgments

We thank the editor and the two anonymous reviewers for their constructive comments. This research was supported by The National Major Project of China [grant number 2017ZX05008007]; and PetroluemChina Project [grant number 2016A-4801].

Appendix A. Supplementary data

Supplementary data to this article can be found online at https://doi.org/10.1016/j.ijrmms.2019.03.012.

References

1. Danial B, Kaveh A, Rahim MS. Modeling of shear wave velocity in limestone by soft computing methods. *Int J Min Sci Technol.* 2017;27(3):423–430. https://doi.org/10.1016/j.ijmst.2017.03.006.
2. Pearson CF, Fehler MC, Albright JN. Changes in compressional and shear wave

velocities and dynamic moduli during operation of a hot dry rock geothermal system. *J Geophys Res - Sol Ea.* 1983;88:3468–3475. https://doi.org/10.1029/JB088iB04p03468.
3. Fernandes RF, Oliveira LFC, Edwards HGM, Brooke CJ, Pepper M. Raman spectroscopic analysis of a belltower commemorative wall decoration. *Appl Phys Mater Sci Process.* 2017;123(2):147. https://doi.org/10.1007/s00339-017-0761-4.
4. Lai H, Wang SY, Wang SY, Xie YL. Experimental research on temperature field and structure performance under different lining water contents in road tunnel fire. *Tunn Undergr Space Technol.* 2014;43(43):327–335https://doi.org/10.1016/j.tust.2014.05.009.
5. Roddy DJ, Younger PL. Underground coal gasification with CCS: a pathway to decarbonising industry. *Energy Environ Sci.* 2010;3(4):400–407. https://doi.org/10.1039/B921197G.
6. Sundberg J, Back PE, Christiansson R, Hökmark M, Ländell M, Wrafter J. Modelling of thermal rock mass properties at the potential sites of a Swedish nuclear waste repository. *Int J Rock Mech Min Sci.* 2009;46(6):1042–1054. https://doi.org/10.1016/j.ijrmms.2009.02.004.
7. Nasseri MHB, Schubnel A, Young RP. Coupled evolutions of fracture toughness and elastic wave velocities at high crack density in thermally treated Westerly granite. *Int J Rock Mech Min Sci.* 2007;44(4):601–616. https://doi.org/10.1016/j.ijrmms.2006.09.008.
8. Nasseri MHB, Tatone BSA, Grasselli G. Fracture toughness and fracture roughness interrelationship in thermally treated Westerly granite. *Pure Appl Geophys.* 2009;166(5-7):801–822. https://doi.org/10.1007/s00024-009-0476-3.
9. Crosby ZK, Gullett PM, Akers SA, Graham SS. Characterization of the mechanical behavior of salem limestone containing thermally-induced microcracks. *Int J Rock Mech Min Sci.* 2018;101:54–62https://doi.org/10.1016/j.ijrmms.2017.11.002.
10. Liu S, Xu JY. Mechanical properties of qinling biotite granite after high temperature treatment. *Int J Rock Mech Min Sci.* 2014;71:188–193https://doi.org/10.1016/j.ijrmms.2014.07.008.
11. Ferrero AM, Marini P. Experimental studies on the mechanical behaviour of two thermal cracked marbles. *Rock Mech Rock Eng.* 2001;34(1):57–66https://doi.org/10.1007/s006030170026.
12. Sun H, Sun Q, Deng WN, Zhang WQ, Chao L. Temperature effect on microstructure and P-wave propagation in linyi sandstone. *Appl Therm Eng.* 2017;115:913–922https://doi.org/10.1016/j.applthermaleng.2017.01.026.
13. Zhang WQ, Sun Q, Zhang YL, Xue L, Kong FF. Porosity and wave velocity evolution of granite after high-temperature treatment, a review. *Environ Earth Sci.* 2018;77(9):350https://doi.org/10.1007/s12665-018-7514-3.
14. Zhang LY, Mao XB, Lu AH. Experimental study on the mechanical properties of rocks at high temperature. *Sci China, Ser A.* 2010;52(3):641–646. https://doi.org/10.1007/s11431-009-0063-y.
15. Koca MY, Ozden G, Yavuz AB, Kincal C, Onargan T, Kucuk K. Changes in the engineering properties of marble in fire-exposed columns. *Int J Rock Mech Min Sci.* 2006;43(4):520–530. https://doi.org/10.1016/j.ijrmms.2005.09.007.
16. Ranjith PG, Viete DR, Chen BJ, Perera MSA. Transformation plasticity and the effect of temperature on the mechanical behaviour of hawkesbury sandstone at atmospheric pressure. *Eng Geol.* 2012;151(151):120–127https://doi.org/10.1016/j.enggeo.2012.09.007.
17. Zhang WQ, Sun Q, Zhu SY, Wang B. Experimental study on mechanical and porous characteristics of limestone affected by high temperature. *Appl Therm Eng.* 2017;110:356–362https://doi.org/10.1016/j.applthermaleng.2016.08.194.
18. Heuze FE. High-temperature mechanical, physical and thermal properties of granitic rocks — a review. *Int J Rock Mech Min.* 1983;20(1):3–10https://doi.org/10.1016/0148-9062(83)91609-1.
19. Zhang F, Zhao JJ, Hu DW, Skoczylas F, Shao JF. Laboratory investigation on physical and mechanical properties of granite after heating and water-cooling treatment. *Rock Mech Rock Eng.* 2017;51(1):677–694https://doi.org/10.1007/s00603-017-1350-8.
20. Xu XC, Liu QS. A preliminary study on basic mechanical properties for granite at high temperature. *Chin J Geotech Eng.* 2000;22(3):332–335.
21. Du SJ, Liu H, Zhi Ht, Chen Hh. Testing study on mechanical properties of post-high-temperature granite. *Chin J Rock Mech Eng.* 2004;23(14):2359–2364.
22. Tian H, Kempka T, Xu NX, Ziegler M. Physical properties of sandstones after high temperature treatment. *Rock Mech Rock Eng.* 2012;45(6):1113–1117. https://doi.org/10.1007/s00603-012-0228-z.
23. Hajpál M, Török Á. Mineralogical and colour changes of quartz sandstones by heat. *Environ Geol.* 2004;46(3-4):311–322. https://doi.org/10.1007/s00254-004-1034-z.
24. Hassanzadegan A, Blöcher G, Milsch H, Urpi L, Zimmermann G. The effects of temperature and pressure on the porosity evolution of flechtinger sandstone. *Rock Mech Rock Eng.* 2014;47(2):421–434. https://doi.org/10.1007/s00603-013-0401-z.
25. Wang G, Qin Y, Shen J, Hu YY, Liu DH, Zhao L. Resistivity response to the porosity and permeability of low rank coal. *Int J Min Sci Technol.* 2016;26(2):339–344https://doi.org/10.1016/j.ijmst.2015.12.022.
26. Dougill JW, Lau JC, Burt NJ. *Toward a Theoretical Model for Progressive Failure and Softening in Rock, Concrete and Similar Material.* Waterloo, W: University of Waterloo Press; 1977.
27. Wang HF, Bonner BP, Carlson SR, Kowallis BJ, Heard HC. Thermal stress cracking in granite. *J Geophys Res Sol Ea.* 1989;94(B2):1745–1758. https://doi.org/10.1029/JB094iB02p01745.
28. Isaak DG. High-temperature elasticity of iron-bearing olivines. *J Geophys Res-Sol Ea.* 1992;97(B2):1871–1885. https://doi.org/10.1029/91JB02675.
29. Aizawa Y, Ito K, Tatsumi Y. Experimental determination of compressional wave velocities of olivine aggregate up to 100°C at 1 Gpa. *Tectonophysics.* 2001;339(3):473–478. https://doi.org/10.1016/S0040-1951(01)00133-0.
30. Zhang WQ, Sun Q, Hao SQ, Wang B. Experimental study on the thermal damage characteristics of limestone and underlying mechanism. *Rock Mech Rock Eng.* 2016;49(8):2999–3008. https://doi.org/10.1007/s00603-016-0983-3.
31. Tian H, Kempka T, Yu S, Ziegler M. Mechanical properties of sandstones exposed to high temperature. *Rock Mech Rock Eng.* 2016;49(1):321–327. https://doi.org/10.1007/s00603-015-0724-z.
32. Gonzalez-Gomez WS, Qunitana P, May-Pat A, Aviles F, May-Crespo J, Alvarado Gil JJ. Thermal effects on the physical properties of limestones from the Yucatan Peninsula. *Int J Rock Mech Min.* 2015;75:182–189. https://doi.org/10.1557/opl.2014.775.
33. Zhang YL, Sun Q, Cao LW, Geng JS. Pore, mechanics and acoustic emission characteristics of limestone under the influence of temperature. *Appl Therm Eng.* 2017;123:1237–1244. https://doi.org/10.1016/j.applthermaleng.2017.05.199.
34. Zhang YL, Sun Q, Geng JS. Microstructural characterization of limestone exposed to heat with XRD, SEM and TG-DSC. *Mater Char.* 2017;134:285–295https://doi.org/10.1016/j.matchar.2017.11.007.
35. Yavuz H, Demirdag S, Caran S. Thermal effect on the physical properties of carbonate rocks. *Int J Rock Mech Min.* 2010;47:94–103. https://doi.org/10.1016/j.ijrmms.2009.09.014.
36. Wu G, Teng NG, Wang Y. Physical and mechanical characteristics of limestone after high temperature. *Chin J Geotech Eng.* 2011;33(2):259–264.
37. Sengun N. Influence of thermal damage on the physical and mechanical properties of carbonate rocks. *Arab J Geosci.* 2014;7:5543–5551. https://doi.org/10.1007/s12517-013-1177-x.
38. Oden JT. *The Finite Elements of Nonlinear Continua.* New York, NY: McGraw-Hill; 1972.
39. Dillon OWJ. A nonlinear thermoelasticity theory. *J Mech Phys Solids.* 1962;10(2):123–131. https://doi.org/10.1016/0022-5096(62)90015-7.
40. Kostek S, Sinha BK, Norris AN. Third-order elastic constants for an inviscid fluid. *J Acoust Soc Am.* 1993;94(5):3014–3017. https://doi.org/10.1121/1.407336.
41. Norris AN, Sinha BK, Kostek S. Acoustoelasticity of solid/fluid composite systems. *Geophys J R Astron Soc.* 2010;118(2):439–446. https://doi.org/10.1111/j.1365-246X.1994.tb03975.x.
42. Wang YZ, Liu D, Wang Q, Shu C. Thermoelastic response of thin plate with variable material properties under transient thermal shock. *Int J Mech Sci.* 2015;104:200–206https://doi.org/10.1016/j.ijmecsci.2015.10.013.l.
43. Wang HG. *The Foundation of Thermal-Elastic.* Bei Jing, BJ: Tsinghua University Press; 1989.
44. Zhao HB, Yin GZ, Chen LJ. Experimental study on effect of temperature on sandstone damage. *Chin J Rock Mech Eng.* 2009;28(s1):2784–2788.
45. Zhang WQ, Qian HT, Sun Q, Chen YH. Experimental study of the effect of high temperature on primary wave velocity and microstructure of limestone. *Environ Earth Sci.* 2015;74(7):1–10. https://doi.org/10.1007/s12665-015-4591-4.
46. Zhao ZK, Sun QZ, Zhang PQ, Jing HO, Sun YM. Phase transformation and expansibility of quartz sands during heating. *J Mater Eng.* 2006;28(10):25–27.
47. Somerton WH. Thermal properties and temperature related behaviour of rock/fluid systems. *J Volcanol Geotherm Res.* 1993;56(1–2):171–172.
48. Zhao P, Xie WH, Wang XS, Gao F. The real time experimental research on rock's sem under high temperature. *Mech Eng.* 2006;28(3):64–67.
49. Chong KP, Hoyt PM, Smith JW, Paulsen BY. Effects of strain rate on oil shale fracturing. *Int J Rock Mech Min.* 1980;17(1):35–43. https://doi.org/10.1016/0148-9062(80)90004-2.
50. Sano O, Ito I, Terada M. Influence of strain rate on dilatancy and strength of oshima granite under uniaxial compression. *J Geophys Res-Sol Ea.* 1981;86(B10):9299–9311. https://doi.org/10.1029/JB086iB10p09299.
51. Masuda K, Mizutani H, Yamada I. Experimental study of strain-rate dependence and pressure dependence of failure properties of granite. *Earth Planets Space.* 1987;35(1):37–66. https://doi.org/10.4294/jpe1952.35.37.
52. Liu S, Xu JY. Mechanical properties of Qinling biotite granite after high temperature treatment. *Int J Rock Mech Min.* 2014;71:188–193. https://doi.org/10.1016/j.ijrmms.2014.07.008.
53. Lockner DA. Rock failure. In: Ahrens TJ, ed. *Rock Physics and Phase Relations, A Handbook of Physical Constants.* Washington, DC: AGU; 1995:127–147.
54. Tang CA, Tham LG, Lee PKK, Tsui Y, Liu H. Numerical studies of the influence of microstructure on rock failure in uniaxial compression — part ii: constraint, slenderness and size effect. *Int J Rock Mech Min Sci.* 2000;37(4):571–583https://doi.org/10.1016/S1365-1609(99)00122-7.
55. Ohnaka M. The quantitative effect of hydrostatic confining pressure on the compressive strength of crystalline rocks. *J Phys Earth.* 1973;21:125–140. https://doi.org/10.4294/jpe1952.21.125.
56. Byerlee JD. Frictional characteristics of granite under high confining pressure. *J Geophys Res.* 1967;72(14):3639–3648. https://doi.org/10.1029/JZ072i014p03639.
57. Yokoyama T, Takeuchi S. Porosimetry of vesicular volcanic products by a water--expulsion method and the relationship of pore characteristics to permeability. *J Geophys Res-Sol Ea.* 2009;114(B2) https://doi.org/10.1029/2008JB005758.
58. Fetter CW. *Contaminant Hydrogeology.* 2th ed. New Jersey, NJ: Prentice-Hall; 1999.
59. Demenico PA, Schwartz FW. *Physical and Chemical Hydrogeology.* New York, NY: Wiley; 1990.
60. Tufail M, Shahzada K, Gencturk B, Wei JQ. Effect of elevated temperature on mechanical properties of limestone, quartzite and granite concrete. *Int J Concr Struct M.* 2017;11(1):1–12. https://doi.org/10.1007/s40069-016-0175-2.
61. Zhao HB, Chen LJ. Experimental study of thermal expansion property of limestone. *Rock Soil Mech.* 2011;32(6):1725–1730. https://doi.org/10.16285/j.rsm.2011.06.016.
62. Engler P, Santana MW, Mittleman ML, Balazs D. Non-isothermal, in situ XRD analysis of dolomite decomposition. *Thermochim Acta.* 1989;140(2):67–76. https://doi.org/10.1016/0040-6031(89)87285-5.